Journal of Materials Chemistry A

ROYAL SOCIETY OF CHEMISTRY

PAPER

View Article Online
View Journal | View Issue

Check for updates

Cite this: *J. Mater. Chem. A*, 2023, **11**, 11341

Engineering polymorphs in colloidal metal dichalcogenides: precursor-mediated phase control, molecular insights into crystallisation kinetics and promising electrochemical activity†

Nilotpal Kapuria, ‡ Niraj Nitish Patil, ‡ Abinaya Sankaran, Fathima Laffir, Hugh Geaney, Edmond Magner, Micheal Scanlon, Kevin M. Ryan and Shalini Singh *

Controlling the crystal phase in layered transition metal dichalcogenides (TMDs) is critical for their diverse, flexible applications. However, due to the thermodynamic stability of 2H over other polymorphs, fine synthesis control over polymorphism in TMDs is challenging, restricting the entire range of characteristics associated with other polymorphs. Herein, we present a solution-based crystal phase engineering approach for layered transition metal disulphide nanosheets by modulating the reactivity of the molecular precursors. By tuning precursor–ligand chemistry, 2H, 1T′ and polytypic MoS_2 and WS_2 are synthesised. The flexibility to selectively modify the reactivity of S and metal precursors allowed control over the proportion of specific phases in synthesised nanosheets. The formation of 1T′ is facilitated by the highly reactive metal and S source, whereas less reactive sources lead to the formation of thermodynamically stable 2H. The electrocatalytic properties of the synthesised TMDs were examined for the oxygen reduction reaction. The polytypic MoS_2 comprising a mix of 2H–1T′ displayed the most positive potential of 0.82 V (*vs.* RHE). The comprehensive mechanistic interpretation of the chemical transformations provided in this study will be instrumental in designing scalable solution-based pathways for phase engineering in layered transition metal dichalcogenides. Furthermore, this synthesis approach has the potential to be extended to various TMD compositions, enabling exquisite control over polymorphism in TMDs.

Received 20th December 2022
Accepted 19th April 2023

DOI: 10.1039/d2ta09892j

rsc.li/materials-a

Department of Chemical Sciences and Bernal Institute, University of Limerick, Limerick, Ireland. E-mail: Shalini.Singh@ul.ie

† Electronic supplementary information (ESI) available. See DOI: https://doi.org/10.1039/d2ta09892j

‡ Nilotpal Kapuria and Niraj Nitish Patil have contributed equally and share joint first author

Dr Shalini Singh is a lecturer in the Department of Chemical Sciences and the Bernal Institute at the University of Limerick, Ireland. She received her PhD in chemistry from the University of Limerick in 2016 and was then an FWO (Research Foundation, Flanders, Belgium) Postdoctoral Fellow at Ghent University, Belgium until 2019. From 2020, she is leading the 'Functional Nanomaterial Research Group' at the University of Limerick. Her research interest is focused on the development of novel colloidal semiconductors and metallic nanocrystals for energy conversion and storage applications.

Introduction

Transition metal dichalcogenides (TMDs) such as MoS_2, WSe_2, ZrS_2, and TiS_2 have emerged as a class of key materials due to their intriguing properties applicable in catalysis, energy storage, electronics, and optoelectronics.[1–4] The TMDs typically occur in 2H or 1T/1T′ crystal phases. The 2H phase displays trigonal prismatic coordination, whereas, in 1T or 1T′, the metal atoms display octahedral coordination.[5] The metal coordination significantly affects the properties of these polymorphs, where the 2H phase is semiconducting in nature and known for its optoelectronic properties.[6] The 1T/1T′ phase outperforms the 2H phase in terms of catalytic activity due to its metallic nature and superior electrical conductivity.[7–9]

From a thermodynamic standpoint, the formation of the 2H phase is more favourable than the formation of the metastable phase like 1T and its derivatives. Most of the synthesis procedures lead to thermodynamically stable 2H phase formation. The octahedral coordination in the 1T phase tends to convert into distorted octahedral coordination resulting in 1T′ or related semi-metallic phases based on the distortion. In this context, the heterogeneities in metal coordination in a single structure will allow effective tuning and switching of physical

and electrical parameters by forming polytypic (mixture of two or more different phases sharing interface) transition metal dichalcogenides. Several techniques have been explored recently for synthesising 1T-TMDs, including exfoliation, plasma hot-electron transfer, electron irradiation, mechanical stresses, and hydrothermal reactions.[10–15] However, the conversion from the 1T/1T′ to the 2H phase is easily triggered by various factors, including contamination, oxidation, and the development of intermediate phases.

Compared to thermodynamically stable phases, metastable TMD materials require higher formation energy, which is challenging to achieve in conventional synthesis approaches like chemical vapour deposition and vapour transport. Traditional high-temperature solid-state procedures do not give enough control to form metastable compounds. These approaches primarily rely on feeding a continuous excessive heat to the reaction vessel to overcome the kinetic barriers of solid-state diffusion, which normally drives the formation of the most thermodynamically stable products.[16] Contrary to this, solution-phase colloidal synthesis approaches allow more kinetic control by attaining an optimum monomer supply rate.[5,17–19] In recent years, colloidal chemistry provided a viable way to obtain metastable phases and thermodynamically stable phases of various metal chalcogenides. The variable phases can be obtained by strategically manipulating the precursor and ligand chemistry to access kinetic growth domains.[20,21] For instance, the metastable wurtzite-like $CuInSe_2$ phase was synthesised over the thermodynamically favoured chalcopyrite phase by slowing down nucleation, using precursors with higher C–Se bond dissociation energy.[22,23] Similarly, several different polymorphs of iron sulfide NCs were synthesised by exploiting the difference in bond dissociation energy of C–S in a series of organosulfur precursors.[24] The interaction of the growing crystal with its chemical environment, which can be tuned in solution phase synthesis, was found to be beneficial in altering the free energy of different polymorphs, lowering the energy barrier for the preferential formation of metastable polymorphs and potentially preventing their transformation into thermodynamically stable ones. For example, coordinating ligands played an important role in the formation of metastable orthorhombic $AgInSe_2$ nanocrystals, and ligand-mediated topotactic cation exchange converts orthorhombic Ag_2Se to orthorhombic $AgInSe_2$.[25] Besides controlling the polymorphism of metal chalcogenide NCs, precursor chemistry has been advantageous in controlling the ratio of different polymorphs. For example, Wang *et al.* showcased that switching between two different selenium precursors (diphenyldiselenide and selenium powder) and keeping a metal precursor the same, polytypic cubic-wurtzite and monophasic cubic phases of Cu_2SnSe_3 NCs were synthesised.[26,27] Recent advancements in colloidal synthesis have led to synthetic colloidal protocols for TMDs forming specific phases, such as 2H, 1T/1T′, by selecting suitable precursors and ligands.[4,28–31] The majority of research relating ligand-precursor coordination to nanocrystal crystal phase has primarily focused on non-layered covalently linked nanocrystallites, and a generic and simple approach for phase engineering in layered van der Waals structures has yet to be established. Further, in terms of catalytic activity, hierarchical heterostructures containing interfacing mixed phases resulted in enhancements in catalytic activity attributed to improved synergistic effects from electrical conductivity and active sites.[32] The studies show that at the heterojunction of the 1T′/2H mixed phase heterostructure, the kinetic barrier drops and electron transport enhances significantly, resulting in an increased number of active sites. In addition to this, the interaction of the 2H phase stabilises the metastable 1T′ phase, considerably increasing its catalytic activity.[33,34] Thus, the control of polytypism and its relationship with electrocatalytic activity tuning requires thorough understanding.

Herein we demonstrate phase engineering of colloidal TMD nanosheets (MoS_2 and WS_2) by tuning precursor reactivity in solution. We showcased that altering the reactivity of metal and S sources resulted in the formation of different polymorphs of monophasic 2H (semiconducting), 1T′ (metallic) transition metal disulfide nanosheets and nanosheets with mixed phase composition (2H–1T′ polytypes). The wide tunable reactivity of the chalcogen precursors facilitated the phase modulation of polytypic transition metal disulfides. Altering the reactivity of the S sources affects the supply rate of S atoms impacting the nucleation rate and favouring the formation of certain polymorphs. Further, the solvent played an important role in controlling the polymorphs; the use of a non-coordinating solvent speeds up reaction kinetics, leading to the formation of a kinetically favourable 1T′ product. In this context, we provide in-depth mechanistic insights that enable improved predictive synthesis of particular phases. In addition, we carried out a retrosynthetic approach that predicted chemical intermediates during the nanosheet formation, leading to the specific polymorph formation. Furthermore, we demonstrate the advantage of the polytypic transition metal sulfide nanosheets over the monophasic nanosheets displaying better catalytic performance with higher onset potentials and diffusion-limited current density during the oxygen reduction reaction (ORR).

Experimental section

Reagents

Molybdenum hexacarbonyl [$Mo(CO)_6$, technical grade, lot# BCBB6657], molybdenum pentachloride ($MoCl_5$, ≥95%, lot# MKCJ9980), tungsten hexacarbonyl [$W(CO)_6$, 97%, lot# MKCD5432], tungsten hexachloride (WCl_6, ≥99.9%, lot# MKCK4583), *tert*-butyl disulphide (TBDS, 97%, lot# 05019EJ), thiourea (≥99%, lot# BCBG6245V), 1-dodecanethiol (1-DDT, ≥98%, lot# STBK4241), oleyl amine (OLA, 70%, lot# STBK3552), squalane (96%, lot# BCCD3542), oleic acid (OA, 90%, lot# MKCH4532), phenyl disulphide (99%, STBC7722V), and trioctylphosphine (TOP, 97%, MKCP6805) were purchased from Sigma Aldrich. Toluene, ethanol, and isopropanol (IPA) were purchased from Lennox, Ireland. Tetradecyl phosphonic acid (TDPA, 97%, AK1803131) was purchased from Plasmachem. KOH pellets (≥85%, lot# L0080) were purchased from Honeywell. All reagents were used as received without further purification.

Table 1 Colloidal synthesis of transition metal disulphides

Reaction no.	Nanocrystal	Solvent (volume)	Metal source	S-source	S-source preparation temperature in °C
R1	MoS_2	OLA (7 ml)	1 eq. $Mo(CO)_6$ in 2 ml OA and 10 mol% TDPA	4 eq. S-powder in 5 ml OLA	100
R1′	WS_2	OLA (7 ml)	1 eq. $W(CO)_6$ in 2 ml OA and 10 mol% TDPA	4 eq. S-powder in 5 ml OLA	100
R2	MoS_2	OA (7 ml)	1 eq. $Mo(CO)_6$ in 5 ml OA and 10 mol% TDPA	4 eq. S-powder in 2 ml TOP	RT
R2′	WS_2	OA (7 ml)	1 eq. $W(CO)_6$ in 5 ml OA and 10 mol% TDPA	4 eq. S-powder in 2 ml TOP	RT
R3	MoS_2	OLA (7 ml)	1 eq. $Mo(CO)_6$ in 2 ml OA and 10 mol% TDPA	4 eq. *tert*-butyl disulphide in 5 ml OLA	RT
R3′	WS_2	OLA (7 ml)	1 eq. $W(CO)_6$ in 2 ml OA and 10 mol% TDPA	4 eq. *tert*-butyl disulphide in 5 ml OLA	RT
R4	MoS_2	OLA (7 ml)	1 eq. $Mo(CO)_6$ in 2 ml OA and 10 mol% TDPA	4 eq. DDT in 5 ml OLA	RT
R4′	WS_2	OLA (7 ml)	1 eq. $W(CO)_6$ in 2 ml OA and 10 mol% TDPA	4 eq. DDT in 5 ml OLA	RT
R5	MoS_2	OLA (7 ml)	1 eq. $Mo(CO)_6$ in 2 ml OA and 10 mol% TDPA	4 eq. thiourea in 5 ml OLA	200
R5′	WS_2	OLA (7 ml)	1 eq. $W(CO)_6$ in 2 ml OA and 10 mol% TDPA	4 eq. thiourea in 5 ml OLA	200
R6	MoS_2	OA (7 ml)	1 eq. $MoCl_5$ in 5 ml OA and 10 mol% TDPA	4 eq. S-powder in 2 ml squalane	140
R6′	WS_2	OA (7 ml)	1 eq. WCl_6 in 5 ml OA and 10 mol% TDPA	4 eq. S-powder in 2 ml squalane	140

Synthesis

Transition metal disulphide nanosheets were prepared using a colloidal hot injection setup. Based on the desired product, using reaction condition Rx (where x = 1–6 in Table 1), the Mo-precursor source was prepared by dissolving 0.25 mmol of $Mo(Co)_6$ or $MoCl_5$ in the desired amount of solvent and 10 mol% of tetradecyl phosphonic acid with subsequent heating to 130 °C on a hotplate kept in an Ar atmosphere in a glovebox. Similarly, under reaction condition Rx' (where x' = 1–6 in Table 1), the metal precursor sources used were $W(Co)_6$ or WCl_6. 1 mmol of a sulphur source was dissolved in the appropriate solvent and prepared as per conditions R (Mo) and R′ (W) as described in Table 1. Both the cationic and anionic precursor sources were prepared and mixed in an oxygen and moisture-free atmosphere at 130 °C. The appropriate volume of solvent was placed in a 3-neck round-bottomed flask and connected to a Schlenk line setup. Table 1 lists the details of the reaction parameters. The precursor solution was evacuated at 120 °C for 20 min and heated to 320 °C under Ar; the mixed solution was injected at a rate of ~0.7 ml min^{-1}. The reaction mixture was kept at 320 °C for 2 h. The NCs were washed in a mixture of 10 ml toluene and 10 ml ethanol at 10 000 rpm for 5 min. After the first wash, the NCs were dispersed in toluene and washed with IPA.

Material characterisation

For transmission electron microscopy (TEM) analysis, the NCs were dispersed in toluene and drop cast on continuous carbon-coated 200 mesh nickel grids (source). Low-resolution and high-resolution TEM (HRTEM) and dark-field scanning transmission electron microscopy (DFSTEM) were conducted on a 200 kV JEOL JEM-2100F field emission microscope, equipped with a Gatan Ultra Scan CCD camera and an EDAX Genesis energy dispersive X-ray spectroscopy (EDS) detector. Interplanar distances and particle orientation were determined from FFT analysis of the selected area in Gatan GMS3 software.

Raman spectroscopy was performed using a Horiba Labraman 300 spectrometer system equipped with a 532 nm laser.

UV-Vis-NIR spectroscopy was done on a Cary 5000 spectrophotometer in cuvettes of 1 cm path length using toluene as solvent.

Electrochemical measurement

Cyclic voltammetry (CV) and linear sweep voltammetry (LSV) experiments for all the synthesized NCs were performed in a standard three-electrode system using catalyst-coated glassy carbon as the working electrode, a platinum wire as a counter electrode, and Ag/AgCl (3 M NaCl) as the reference electrode in 0.1 M KOH solution. The studies were performed using the rotating disk electrode (RDE) setup, and the PGSTAT204 potentiostat was from Metrohm (Netherlands) and used in conjunction with NOVA software version 2.1.2. Approximately 3.55 mg of the NC catalyst was homogeneously dispersed in 300 μl of ethanol, 100 μl of IPA, and 25 μl of 5 wt% Nafion (binder) by 60 min ultrasonication forming casting ink. 4 μl of this prepared ink is drop cast upon the pre-polished glassy carbon electrode to form a 0.5 mg cm^{-2} active catalyst layer. Cyclic voltammetry studies were performed in both O_2 and N_2 saturated 0.1 M KOH solution at a scan rate of 50 mV s^{-1} over the potential range of −1 to 0.2 V (*vs.* Ag/AgCl (3 M NaCl)). The recorded potentials are reported *vs.* the reversible hydrogen

electrode (RHE) by converting them using the following Nernst equations, where $E^{o}_{Ag/AgCl}$ (3 M NaCl) = 0.1976 V *vs.* the standard hydrogen electrode (SHE) at 25 °C:

$$E_{RHE} = E_{Ag/AgCl} + 0.059pH + E^{o}_{Ag/AgCl(3\ M\ NaCl)} \quad (1)$$

At different rotation rates from 400 to 2400 rpm, linear sweep voltammograms were recorded using O_2 saturated 0.1 M KOH solution at a scan rate of 5 mV s^{-1} over the potential range of 0.2 to −1 V (*vs.* Ag/AgCl (3 M NaCl)) to understand the diffusion kinetics of the catalyst layer.[35] The Koutechy–Levich (K–L) plots were derived from the LSV curves using the following equations:

$$1/j = 1/j_l + 1/j_k = 1/B\omega^{1/2} + 1/j_k \quad (2)$$

$$j_k = nFkC_0$$

$$B = 0.62nFC_0D_0^{-2/3}v^{-1/6}$$

where j is the measured current density, j_k is the kinetic-limiting current, and ω is the angular velocity, n is the number of electrons involved in the ORR, F is Faraday's constant (96 485 C mol^{-1}), k is the electron transfer rate constant, $C_0 = 1.2 \times 10^{-6}$ mol cm^{-3} is the concentration of O_2 molecules in 0.1 M KOH, $D_0 = 1.90 \times 10^{-5}$ cm^2 s^{-1} is the diffusion coefficient of O_2 in pure water at 25 °C and 1.0 atm O_2 pressure, and $v = 0.01$ cm^2 s^{-1} is the kinematic viscosity of 0.1 M KOH.[36] For the stability test, the polytypic NCs were cycled for a longer duration under the same conditions mentioned above. LSVs were recorded at 1600 rpm under similar conditions as above after 2500 CV cycles for MoS_2 polytypic NCs and 1000 cycles for WS_2 polytypic NCs.

Results and discussion

Synthesis of TMD nanosheets

Using a controlled injection (~0.7 ml min^{-1}) of metal source dissolved in oleic acid (OA) and added with S-source mixed in a range of hot co-ordinating and non-coordinating solvents resulted in the formation of MS_2 NCs with different percentages

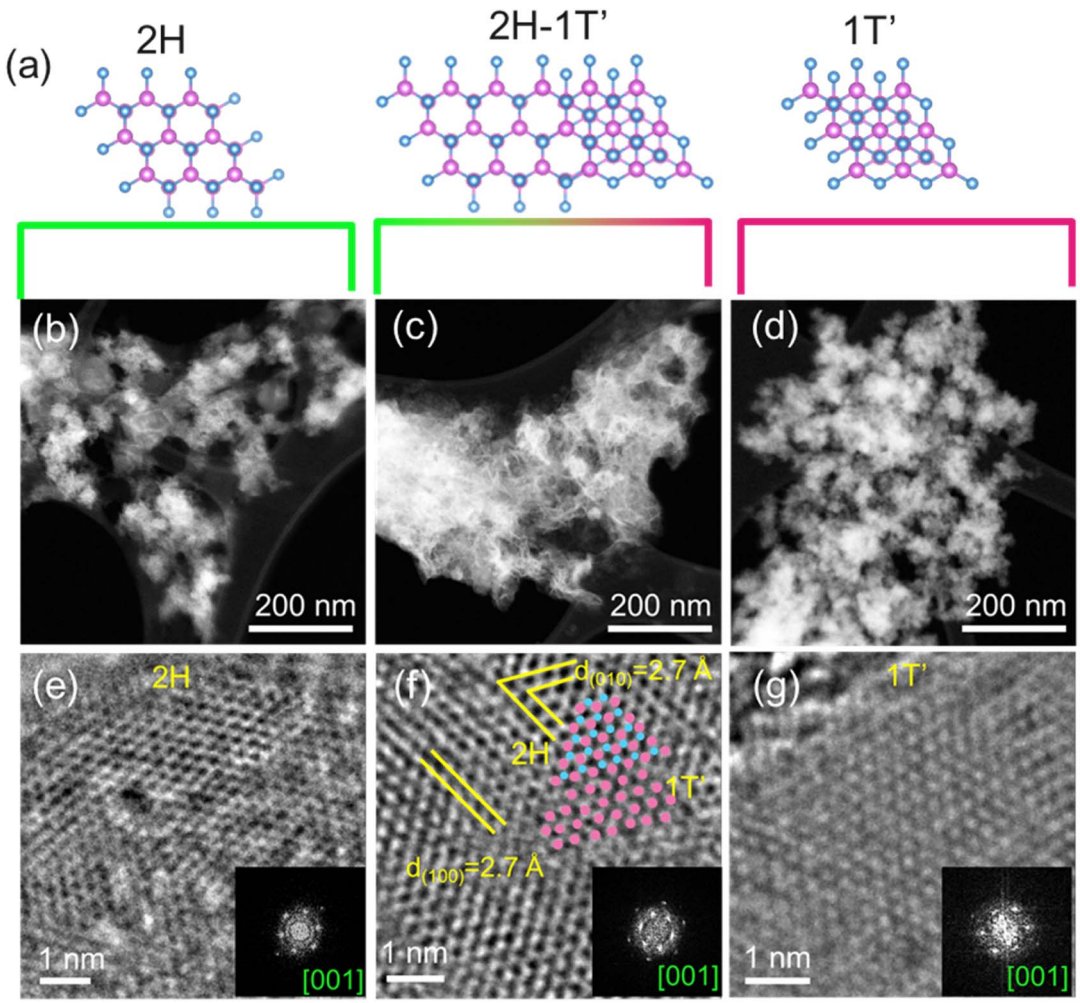

Fig. 1 (a) Schematic showing the atomic arrangement of 2H, 2H–1T′ polytype, and 1T′ TMDs projected from the *c*-axis, the blue atoms correspond to S and pink atoms correspond to Mo or W; low magnification STEM micrograph of MoS_2 NCs prepared under conditions (b) R1, (c) R3, (d) R6 and the corresponding HRTEM images for the (e) 2H phase, (f) 2H–1T′ phase and (g) 1T′ phases of MoS_2 prepared under conditions R1, R3 and R6 respectively.

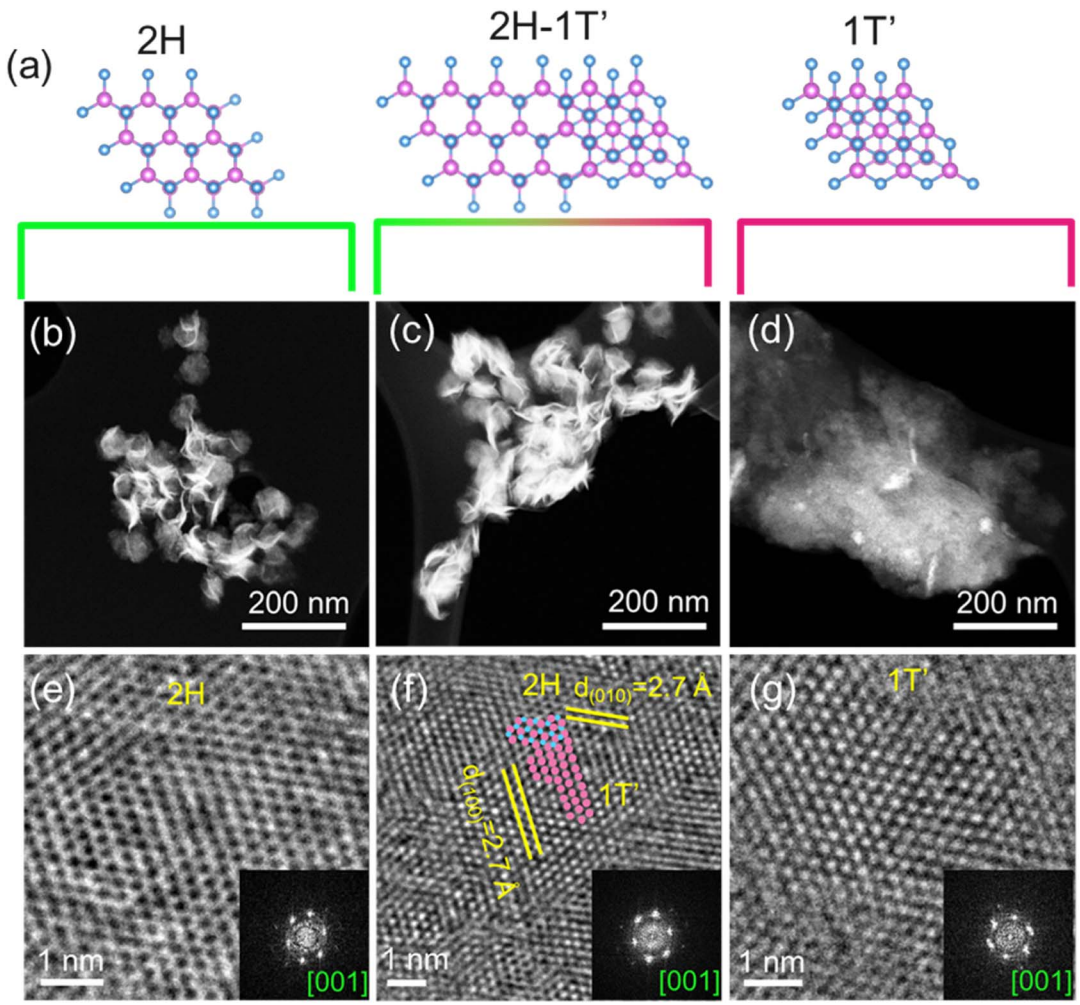

Fig. 2 (a) Schematic showing the atomic arrangement of 2H, 2H–1T′ polytype, and 1T′ TMDs projected from the *c*-axis low magnification STEM micrograph of WS_2 NCs prepared under conditions (b) R1′, (c) R3′, (d) R6′ and the corresponding HRTEM images for the (e) 2H phase dominated WS_2 where pink patches denote the 1T′ phase, (f) 2H–1T′ phase and (g) 1T′ dominated phases of WS_2 where green patches denote the 2H phase prepared under conditions R1′, R3′, and R6′, respectively.

of 2H and 1T′ phases. Based on the reactivity of different metals and S-sources, a series of reactions were carried out as listed in Table 1 to control the percentage of a particular crystal phase in polytypic MS_2 NCs (see the Experimental section for details). Annular dark-field scanning electron micrographs (ADF-STEM) (Fig. 1b–d and 2b–d, ESI S1†) of the MoS_2 and WS_2 nanocrystals (NCs) display nanosheet-like morphologies where multiple layers are bundled together. The contrast in symmetry of the trigonal coordinated 2H phase and octahedral coordinated 1T′ phase of the TMD is identified by the high-resolution TEM (HRTEM) of the NCs (Fig. 1a, e–g, and k–m).

For MoS_2, the HRTEM of the NCs synthesized using S–OLA in condition R1 showcases a honeycomb-like atomic arrangement with a *d*-spacing of 2.7 Å corresponding to the (100) and (010) planes which are characteristic features for 2H phase (Fig. 1e). Suspension of S powder in non-coordinating solvent squalane in synthesis R6 resulted in 1T′ phase formation with octahedral Mo–S coordination where the nearest Mo–Mo distance is 3.2 Å as calculated from HRTEM (Fig. 1g). The alternating Mo–Mo distance of 2.7 Å along with the typical Mo–Mo distance of 3.2 Å as shown in the ESI† (Fig. S2a†) explains the distortion present in the Mo–S octahedral coordination in the 1T′ structure. Using *tert*-butyl disulfide (TBDS) in condition R3, the presence of both 2H and 1T′ phases is observed in the MoS_2 nanosheets as shown in Fig. 1f. Similarly, for WS_2, conditions R1′, R3′, and R6′ resulted in 2H dominated, a mixed 2H–1T′ and 1T′ dominated phases respectively (Fig. 2e–g). Furthermore, in UV-Vis-NIR absorption spectra (Fig. S3†), the 2H MoS_2 and 2H-dominated WS_2 exhibit three excitonic peaks. The intensity of these peaks is reduced in the polytypic 2H–1T′ phases of MoS_2 and WS_2, whereas the absorbance appears to be featureless in the spectra of 1T′ phases of MoS_2 and WS_2.

Polytypism

The effect of S-precursor reactivity on polytypism of the 2H–1T′ phase was studied using Raman spectra and XPS analysis of the as-synthesised nanosheets. The presence of the peaks at 378 (E^1_{2g}) and 405 (A_{1g}) cm^{-1} (Fig. 3a) for MoS_2 confirms the

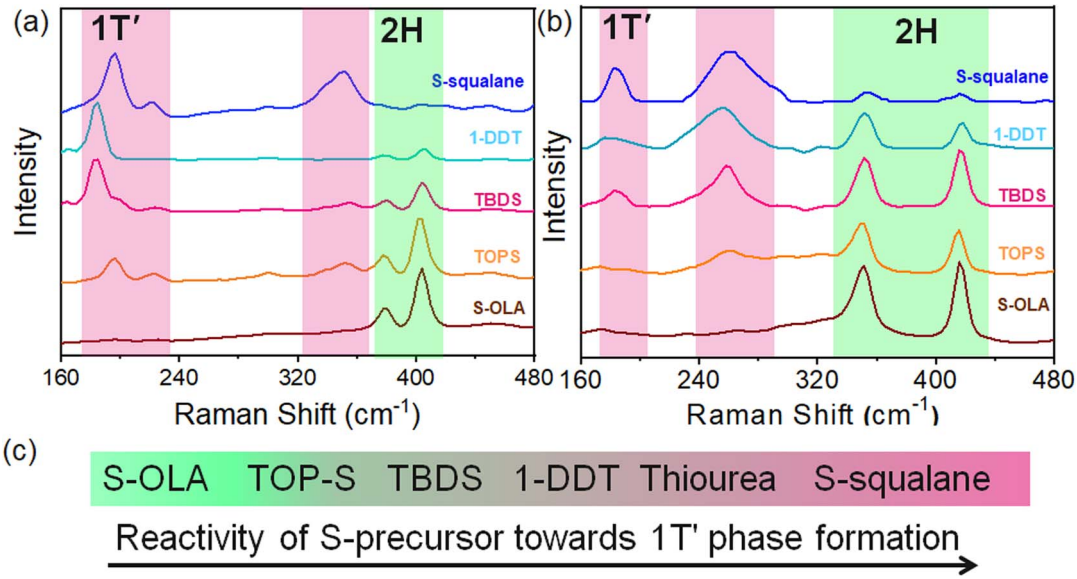

Fig. 3 Raman spectra of (a) MoS_2 and (b) WS_2 NCs prepared by manipulation of precursor chemistry of S and the metal source; (c) reactivity trend of S-sources follow S–OLA (R1, R1′) < TOP–S (R2, R2′) < TBDS (R3, R3′) < 1-DDT (R4, R4′) < S–squalane (R6, R6′) for 1T′ phase formation.

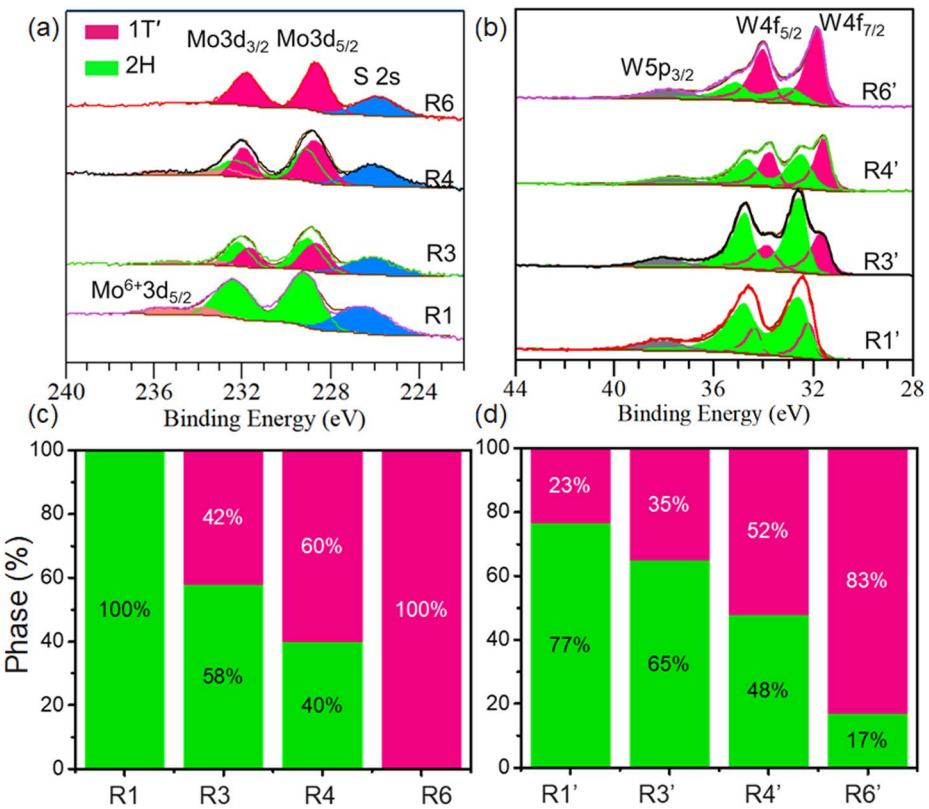

Fig. 4 XPS analysis of as prepared (a) MoS_2 NCs, (b) WS_2 NCs synthesized using different S-sources and metal sources; phase percentage analysis of (c) MoS_2 and (d) WS_2 from deconvolution of the XPS spectra.

formation of the 2H phase when S–OLA is used with $Mo(CO)_6$. Similar reaction conditions for WS_2 display 2H rich phase with Raman peaks 350 (E^1_{2g}) and 415 (A_{1g}) (Fig. 3b). The diminished intensity of these two peaks with the appearance of peaks at 185–195 and 225 cm^{-1} corresponding to the phonon modes and a peak at 350 cm^{-1} (J_3) indicates the formation of the 1T′-phase

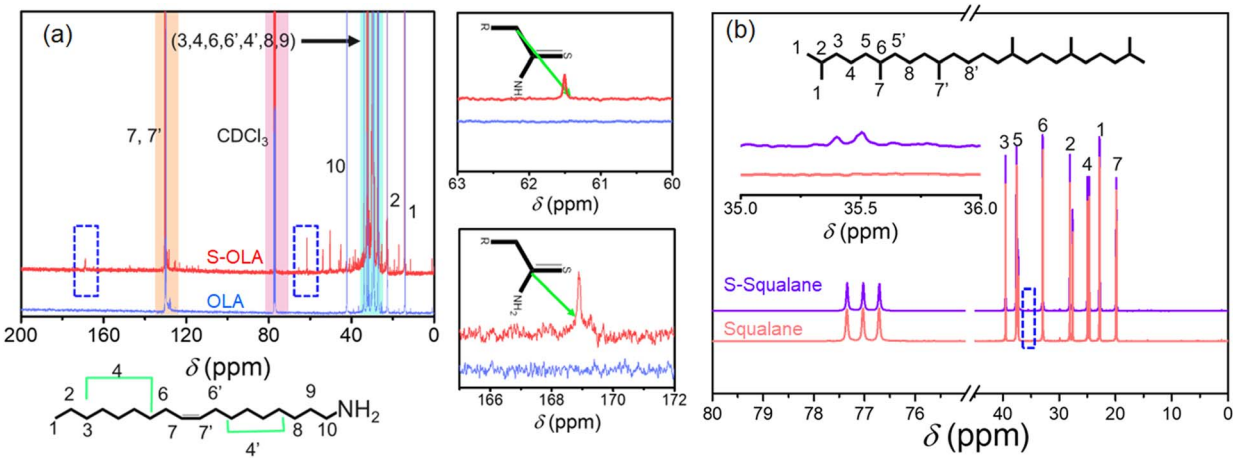

Fig. 5 ^{13}C NMR of (a) S–oleylamine solution and (b) S–squalane suspension heated under reaction conditions. $CDCl_3$ used as a reference displays a peak at ~77.2 ppm.

MoS_2 when S–squalane is used with $MoCl_5$.[37,38] Additionally, a less intense peak at ~300 cm^{-1} (E_{1g}) suggests the occurrence of octahedral Mo–S coordination.[30] Similarly, for WS_2 nanocrystals, the appearance of 180 cm^{-1} peaks resulting from phonon mode and 267 cm^{-1} (J_2) peak and suppression of (E^1_{2g}) and A_{1g} peaks indicate the occurrence of the 1T′ phase (Fig. 3b).[30] Gradual increase of reactivity of S-source induced polytypism in nanosheets with increased 1T′ phase formation when TOP–S, TBDS, and 1-DDT are used as the S-source (Fig. 3c). For MoS_2, the peaks at 228.5 ($3d_{5/2}$) and 231.6 eV ($3d_{3/2}$) correspond to the 1T′ phase whereas the characteristic peaks of 2H MoS_2 phase appear at 229.2 (Mo $3d_{5/2}$) and 232.3 eV (Mo $3d_{3/2}$) (Fig. 4a). For 1T′ WS_2, the characteristic W4f peaks correspond to 31.5 ($W4f_{7/2}$) and 33.7 eV ($W4f_{5/2}$) with a binding energy of 0.9 eV lower than the 2H phase (Fig. 4b). Upon deconvolution of the XPS spectra, the 1T′ phase percentage with respect to the 2H phase is determined (Fig. 4c and d). When highly reactive S–squalane and WCl_6 were employed, the metastable phases of MS_2 nanocrystals are achieved by establishing kinetic growth conditions. The monomer supply rate generally decides the reaction kinetics. We utilized the reactivity differences of the commercially available S-sources to avail active sulphur species to control the metastable phase formation. The most commonly used S-source, S powder occurs as polysulphide (S_n). Upon the reaction with OLA, it undergoes S–S scission to form radical anions and alkanethioamide as per eqn (3).[39] To understand the growth condition, S–OLA solution was heated to 320 °C under reaction condition R1 and analysed with ^{13}C NMR. The presence of the peak at ~169 ppm from C of C=S centre and the peak at ~61 ppm from the α-C of $RCH_2C{=}SNH_2$ support the formation of alkanethioamide (Fig. 5a). Furthermore, in the ^{1}H NMR, the α-proton peak diminishes after alkanethioamide formation (Fig. S7†). This rate-limiting step is responsible for a slow rate of sulphide species formation during MS_2 synthesis.

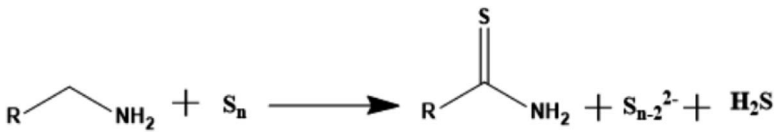

(3)

synthesis resulted in 100% of 1T′ MoS_2 and 83% of 1T′ WS_2 phase formation (R6 and R6′). The estimated 1T′ phase % in the NCs synthesized using TBDS and $W(CO)_6$ is 36 and 35%, respectively, for MoS_2 and WS_2 (R3 & R3′). When 1-DDT is used as the S source with metal carbonyls, the 1T′ phase % further increases beyond 50% of the phase composition (R4 & R4′).

Mechanistic insights

We have investigated the role of precursor–ligand chemistry in modulating the TMD nanosheets' crystal phases. The

Here, the direct use of alkanethioamide or thioamide group will expedite the monomer supply rate. To increase the lability of the –C=S in thioamides, an electron-donating group such –NH_2 (*e.g.*, thiourea) will further facilitate the reaction kinetics as illustrated in eqn (4). As a result, more of the 1T′ phase forms when thiourea is used as the S-source as observed in the XPS spectra of the TMDs (Fig. S6†).

The reactivity of the C–S bond can be further varied using organyl disulfide sources. Reactivity in organyl disulphides varies depending on the bond dissociation energy of C–S. The

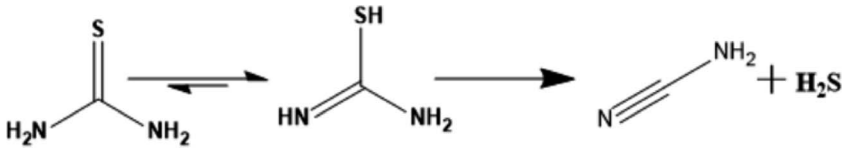

(4)

tert-butyl disulphide (TBDS), which displays C–S bond dissociation energies (BDE) of ~58 kcal mol^{-1}, undergoes a slow process to produce S_2^{2-} species preceding a sluggish sulphide species formation reaction.[40] When S powder is used with TOP, the strong interaction of TOP with S (TOP=S) slows the free sulphide formation.[41] However, adding excess oleic acid facilitates the S^{2-} formation from TOP–S as per eqn (5), making it more reactive than S–OLA but less reactive than *tert*-butyl disulphide. Similar to TBDS, 1-DDT shows C–S BDE between ~55 and 60 kcal mol^{-1}. However, the presence of OLA forms a Lewis acid–base adduct ($R1CH_2C–S^{\delta-}–H^{\delta+}\cdots NH_2R$) with 1-DDT, increasing the reactivity of the thiol compared to TBDS.

confirmed from the Raman spectra of the nanosheets formed using metal chlorides (Fig. S4 and S5†). Considering the reaction outcome and reactivity trend of precursors, we propose that MS_2 nucleation initiates with metastable 1T′ phase formation. Hence, manipulation of precursor chemistry which would allow a faster rate of free sulphide species (S_n^{2-}) and free metal cation (M^{n+}) formation will ultimately arrest the distorted octahedral M–S coordination of the kinetically metastable phase – 1T′. For example, 1T′ phase formation dominates when S–squalane is used with reactive MCl_x. In contrast, when S–squalane or thiourea (Fig. S6†) is replaced with a less reactive S–OLA or TBDS, a slow monomer supply rate provides ample time for

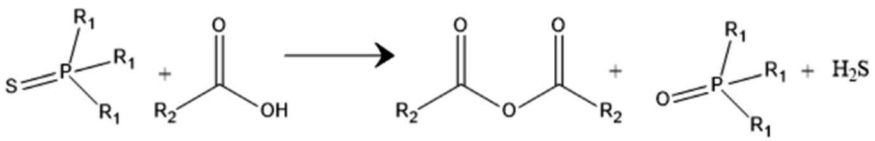

(5)

In contrast to the previous systems, squalane as a non-coordinating solvent does not show any interaction with the sulphur source; hence it tends to supply a high amount of S_n^{2-}. A possible side reaction based on the millimolar concentration of sulfur radicals is forming alkyl disulphide or alkanethiols when reacting with alkane, as shown in eqn (6).

$$RH + S_n^{\cdot} \rightarrow R^{\cdot} + S_nH \xrightarrow{S_n^{\cdot}} RS_n^{\cdot} \xrightarrow{RH} RS_nH + R^{\cdot} \xrightarrow{RS_n^{\cdot}} RS_nR \quad (6)$$

The presence of the alkyl thiol was confirmed from the ^{13}C NMR peak around ~36 ppm (Fig. 5b). The formed alkyl thiol will also stabilize the metastable form. Thus, S-sources' reactivity follows the following trend: S–squalane > thiourea > *tert*-butyl disulfide > TOP–S > S–OLA.

Furthermore, a comprehensive picture of the influence of precursor–ligand coordination on the crystallinity of the nanosheets can only be built when the metal sources are considered. Among the utilised metal sources in this study, metal carbonyls are comparatively less reactive than metal chlorides due to the ability to exert readily available metal cations than the metal carbonyl, where a π M → CO back bonding exists.[42] Thus, employing metal chlorides as a precursor favours a greater monomer supply rate forming 1T′ dominated polytypes as reorganisation of octahedral M–S co-ordination to form 2H phase dominated TMDs. Hence, the reaction trend of R1 < R2 < R3 < R4 < R5 < R6 is observed towards a faster nucleation rate, resulting in the formation of 1T′ dominated phases.

Furthermore, to check our hypothesis, the aliquots from reactions of MoS_2 performed with four different S-sources with variable reactivity (S–OLA < TBDS < 1-DDT < S–squalane) were collected at different growth times of 1, 5, 10, 30, 60 min at 320 °C and were screened with UV-Vis-NIR absorption spectroscopy. All the aliquots collected at 1 min showed the presence of 1T′ phase irrespective of the S-sources used (Fig. 6). However, for low reactive S-sources such as S–OLA, the formation of the 2H-phase started just after 5 min of growth time. TBDS shows higher reactivity than S–OLA; thus, the formation of the 2H phase occurs after 10 min. Further increased reactivity realised using 1-DDT exhibited 2H phase formation only after 30 min of growth time. However, the reaction system using highly reactive S–squalane and $MoCl_5$ did not exhibit any occurrence of the 2H phase even after 60 min of growth time.

Ostwald's step rule for nucleation suggests that a metastable phase forms first before it's conversion into a thermodynamically stable phase.[43] Thus, in the mentioned systems, the 1T′ phase forms first as the metastable phase, as shown in

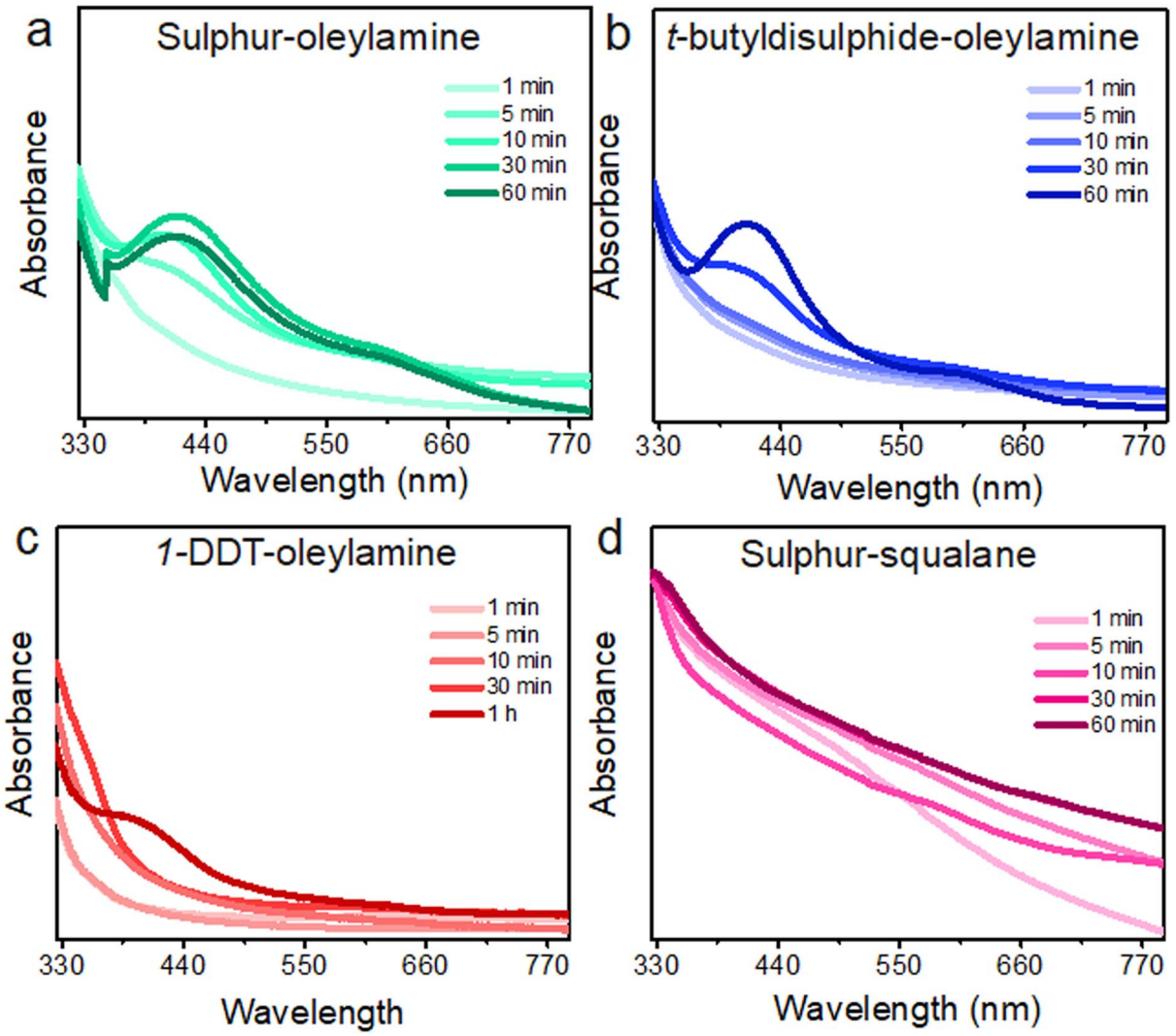

Fig. 6 UV-Vis-NIR spectra of MoS_2 reaction aliquots withdrawn at 1, 5, 10, 30, and 60 min of growth time at 320 °C using (a) S–squalane and $MoCl_5$, (b) 1-DDT–oleylamine and $Mo(CO)_6$, (c) TBDS–oleylamine and $Mo(CO)_6$, and (d) $Mo(CO)_6$, and S–OLA suspension.

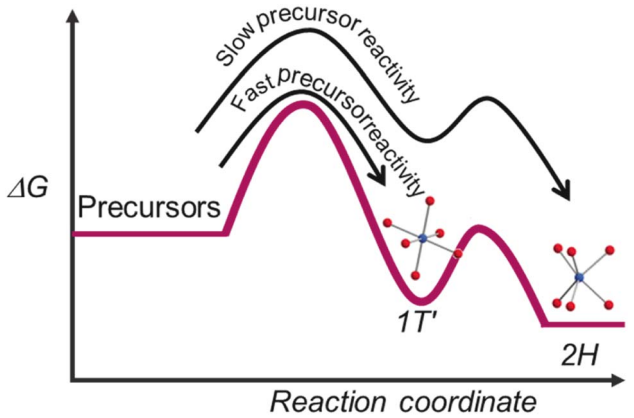

Scheme 1 Representation of transition metal disulphide formation based on precursor reactivity trends. The blue spheres denote metal, and the red spheres represent sulphur.

Scheme 1. The slower reactivity S-source provided enough time for the distorted M–S octahedral coordination to re-organise into stable trigonal prismatic M–S coordination as in the 2H phase. However, higher reactivity of the S-source arrests the distorted octahedral M–S co-ordination *via* continuous supply of S-monomer, preventing re-organisation into trigonal prismatic coordination.

Electrochemical performance

We study the ORR activity of synthesized 2H, 1T′, and polytypic 2H–1T′ MS_2 NCs in alkaline media using CV and LSV techniques. The LSV curves of MoS_2 polymorphs recorded in an O_2 saturated environment at 1600 rpm show that polytypic 2H–1T′ MoS_2 has superior ORR kinetics, with an onset potential, E_0 = 0.82 V *vs.* RHE compared to 2H MoS_2 (E_0 = 0.76 V *vs.* RHE) and 1T′ MoS_2 (E_0 = 0.79 V *vs.* RHE), see Fig. 7a. In addition, the polytypic 2H–1T′ MoS_2 exhibits a ~35 mV positive shift in half-

wave potential and a higher diffusion-limited current density (j_L = −3.5 mA cm^{-2}) compared to 1T′ MoS_2 (j_L = −1.8 mA cm^{-2}).

A similar trend is observed for WS_2 nanosheet samples where the onset potential for polytypic 2H–1T′, 1T′, and 2H WS_2 is 0.79, 0.77, and 0.74 V *vs.* RHE, respectively (Fig. 7b). The polytypic 2H–1T′ WS_2 exhibits a ∼41 mV positive shift in half-wave potential and a higher diffusion-limited current density (j_L = −2.2 mA cm^{-2}) compared to 1T′ MoS_2 (j_L = −1.5 mA cm^{-2}). Though 2H MS_2 is a more stable structure, the active sites are only located at the edges leading to poor electrochemical activity. In contrast, the 1T′ phase exhibits metallic behaviour where both the basal sites and edges are active towards molecular intermediate binding during electrocatalysis.[44] As a result, 1T′ nanosheets display better catalytic activity but suffer from poor stability. Phase engineering of the MS_2 to form polytypic NCs results in enhanced electrocatalytic activity with onset values comparable to most reports (Table S2†).[45,46] In our study, we see improved reduction kinetics for the polytypes as the integration of the 1T′ phase is beneficial to improve the number of active sites and electronic conductivity and the 2H phase provides stability to the 1T′ phase.[47] Additionally, the interface between 2H–1T′ can show chalcogen vacancies and accumulated charges inducing enhanced charge transfer beneficial for improved ORR kinetics, thus, performing better than the monophases.[48–50] This was further corroborated by decreased Tafel slope values of the polytypes compared to 1T′ monophases (Fig. S9†). Additionally, the MoS_2 polytype shows improved stability while maintaining its polytypic nature during the long-term cycling of ORR, as shown in Fig. S10 and S11a.† However, in the case of WS_2, though the mixed phase is maintained (Fig. S11b†), a slight negative shift in onset potential and half-wave potential is observed (Fig. S10b†) because of structural deterioration as confirmed in post-mortem TEM analysis (Fig. S12†).

The corresponding CVs of the best performing polytypic 2H–1T′ MoS_2 (Fig. 7c) and 2H–1T′ WS_2 (Fig. 7d) recorded in an O_2 or N_2 saturated 0.1 M KOH electrolyte are shown. The diffusion peaks observed in an O_2-saturated environment with onset potential values of 0.82 *vs.* RHE (2H–1T′ MoS_2) and 0.79 V *vs.* RHE (2H–1T′ WS_2) represent the catalytic reduction of O_2. The absence of a reduction peak in the CV scans in a N_2 saturated environment confirms the oxygen reduction activity of the NCs.

Linear sweep voltammograms of MS_2 NCs recorded in an O_2 environment at different rotational speeds from 400 to 2400 rpm are shown in Fig. S8a and c.† The current densities are independent of the rotation speed between 0.9 and 0.85 V *vs.* RHE, which indicates kinetic current density (j_k). The diffusion current density increases with the rotation speed between 0.6

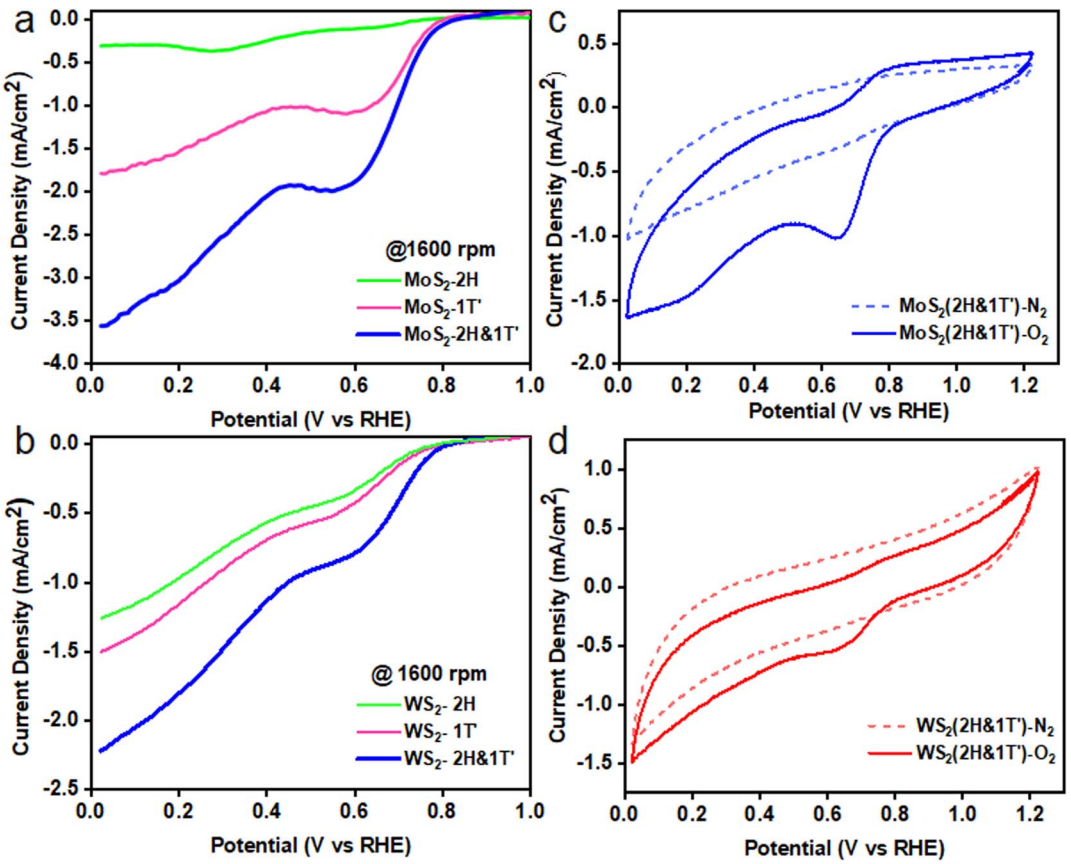

Fig. 7 ORR activity of MoS_2 and WS_2 samples. Rotating disc voltammograms (at 1600 rpm) of (a) 2H-, 1T′- and polytypic 2H–1T′ MoS_2 NCs, and (b) 2H-, 1T′- and polytypic 2H–1T′ WS_2 NCs in O_2 saturated 0.1 M KOH at 1600 rpm; cyclic voltammograms of (c) polytypic 2H–1T′ MoS_2 and (d) 2H–1T′ WS_2 in O_2 and N_2 saturated 0.1 M KOH.

and 0.45 V *vs.* RHE. This increase in the current density at increased rotating speed is due to the reduced capacitance between the electrode surface and reactant, a high O_2 diffusion rate, and mass transfer. The corresponding K–L plot was drawn from the LSV curves to understand the order of the reaction. MS_2 (MoS_2 and WS_2). The number of electrons (n) transferred per O_2 molecule during the ORR increases from 2.67 to 3.94 for MoS_2 (Fig. S8b†) and 2.37 to 4.30 for WS_2 (Fig. S8d†) in the potential range of 0.6 to 0.2 V. Thus, it corroborates the 2nd order reaction kinetics involving a 2-electron process as per the following pathways:[51]

$$O_2 + H_2O + 2e^- \rightarrow OH^- + HO_2^- \quad (7)$$

$$H_2O + HO_2^- + 2e^- \rightarrow 3OH^- \quad (8)$$

The synthesized MS_2 MoS_2 and WS_2 NCs exhibit the sluggish 2-electron peroxide pathway rather than a faster 4-electron pathway like Pt–C, as reported in several other studies.[52] Yet, the phase engineering has led to the enhanced degree of activation owing to interfacing 2H–1T' phases present in the polytypic nanosheets.[53] The controlled reaction to form polytypic MoS_2 nanosheets showed an increase in the number of electrons transferred (Fig. S8b and d†), leading to better reduction kinetics than the WS_2 nanosheets.

Conclusions

In summary, alteration of precursor reactivity is demonstrated as an effective phase control tool for layered transition metal disulphide NC synthesis. Our system exploits the difference in reactivity of a series of commercially available S-sources which displayed a reactivity trend of S–OLA < TOP–S < *tert*-butyl sulphide < 1-DDT < S–squalane towards controlled 1T′ phase formation. Similarly, reactive metal sources such as metal chlorides displayed a higher tendency to form 1T′ phases than metal carbonyls. The significance of polytypism is realised by applying these NCs as electrode materials for the oxygen reduction reaction where the polytypes showed superior performance compared to the monophasic counterparts. The polytypic MoS_2 displayed a higher onset potential of 0.82 V (*vs.* RHE) with a current diffusion limited density of -3.5 mA cm^{-2} and polytypic WS_2 displayed an onset potential of 0.79 V (*vs.* RHE) with a current diffusion limited density of -2.2 mA cm^{-2}. The present study provides important insights into chalcogen precursor reactivity regulation to create a suitable library of polytypic TMS NCs to significantly enhance the physiochemical properties without foreign metal doping.

Conflicts of interest

There are no conflicts to declare.

Acknowledgements

NK acknowledges funding from the Irish Research Council (IRC) under Grant Number IRCLA/2017/285. NNP acknowledges the funding from the Faculty of Science and Engineering, University of Limerick. K. M. R. acknowledges Science Foundation Ireland (SFI) under the Principal Investigator Program under contract no. 16/IA/4629 and under grant no. SFI 16/M-ERA/3419. S. S. acknowledges the funding and support from the Department of Chemical Sciences, University of Limerick.

References

1 C. L. Tan, X. H. Cao, X. J. Wu, Q. Y. He, J. Yang, X. Zhang, J. Z. Chen, W. Zhao, S. K. Han, G. H. Nam, M. Sindoro and H. Zhang, Recent Advances in Ultrathin Two-Dimensional Nanomaterials, *Chem. Rev.*, 2017, **117**, 6225, DOI: **10.1021/acs.chemrev.6b00558**.

2 C. L. Tan and H. Zhang, Two-dimensional transition metal dichalcogenide nanosheet-based composites, *Chem. Soc. Rev.*, 2015, **44**, 2713, DOI: **10.1039/c4cs00182f**.

3 P. S. Zhou, G. Collins, Z. Hens, K. M. Ryan, H. Geaney and S. Singh, Colloidal WSe2 nanocrystals as anodes for lithium-ion batteries, *Nanoscale*, 2020, **12**, 22307.

4 P. S. Zhou, P. Schiettecatte, M. Vandichel, A. Rousaki, P. Vandenabeele, Z. Hens and S. Singh, Synthesis of Colloidal WSe2 Nanocrystals: Polymorphism Control by Precursor-Ligand Chemistry, *Cryst. Growth Des.*, 2021, **21**, 1451, DOI: **10.1021/acs.cgd.0c01036**.

5 A. Coogan and Y. K. Gun'ko, Solution-based "bottom-up" synthesis of group VI transition metal dichalcogenides and their applications, *Mater. Adv.*, 2021, **2**, 146, DOI: **10.1039/d0ma00697a**.

6 K. F. Mak and J. Shan, Photonics and optoelectronics of 2D semiconductor transition metal dichalcogenides, *Nat. Photonics*, 2016, **10**, 216, DOI: **10.1038/Nphoton.2015.282**.

7 M. A. Lukowski, A. S. Daniel, F. Meng, A. Forticaux, L. S. Li and S. Jin, Enhanced Hydrogen Evolution Catalysis from Chemically Exfoliated Metallic MoS2 Nanosheets, *J. Am. Chem. Soc.*, 2013, **135**, 10274, DOI: **10.1021/ja404523s**.

8 D. Voiry, M. Salehi, R. Silva, T. Fujita, M. W. Chen, T. Asefa, V. B. Shenoy, G. Eda and M. Chhowalla, Conducting MoS2 Nanosheets as Catalysts for Hydrogen Evolution Reaction, *Nano Lett.*, 2013, **13**, 6222, DOI: **10.1021/nl403661s**.

9 G. Q. Li, D. Zhang, Q. Qiao, Y. F. Yu, D. Peterson, A. Zafar, R. Kumar, S. Curtarolo, F. Hunte, S. Shannon, Y. M. Zhu, W. T. Yang and L. Y. Cao, All The Catalytic Active Sites of MoS2 for Hydrogen Evolution, *J. Am. Chem. Soc.*, 2016, **138**, 16632, DOI: **10.1021/jacs.6b05940**.

10 C. Lee, Q. Y. Li, W. Kalb, X. Z. Liu, H. Berger, R. W. Carpick and J. Hone, Frictional Characteristics of Atomically Thin Sheets, *Science*, 2010, **328**, 76, DOI: **10.1126/science.1184167**.

11 Y. M. Kang, S. Najmaei, Z. Liu, Y. J. Bao, Y. M. Wang, X. Zhu, N. J. Halas, P. Nordlander, P. M. Ajayan, J. Lou and Z. Y. Fang, Plasmonic Hot Electron Induced Structural Phase Transition in a MoS2 Monolayer, *Adv. Mater.*, 2014, **26**, 6467, DOI: **10.1002/adma.201401802**.

12 Y. C. Lin, D. O. Dumcencon, Y. S. Huang and K. Suenaga, Atomic mechanism of the semiconducting-to-metallic phase transition in single-layered MoS2, *Nat. Nanotechnol.*, 2014, **9**, 391, DOI: **10.1038/Nnano.2014.64**.

13 F. Dybala, M. P. Polak, J. Kopaczek, P. Scharoch, K. Wu, S. Tongay and R. Kudrawiec, Pressure coefficients for direct optical transitions in MoS2, MoSe2, WS2, and WSe2 crystals and semiconductor to metal transitions, *Sci. Rep.*, 2016, **6**, 26663, DOI: **10.1038/srep26663**.

14 A. P. Nayak, S. Bhattacharyya, J. Zhu, J. Liu, X. Wu, T. Pandey, C. Q. Jin, A. K. Singh, D. Akinwande and J. F. Lin, Pressure-induced semiconducting to metallic transition in multilayered molybdenum disulphide, *Nat. Commun.*, 2014, **5**, 3731, DOI: **10.1038/ncomms4731**.

15 X. M. Geng, Y. L. Zhang, Y. Han, J. X. Li, L. Yang, M. Benamara, L. Chen and H. L. Zhu, Two-Dimensional Water-Coupled Metallic MoS2 with Nanochannels for Ultrafast Supercapacitors, *Nano Lett.*, 2017, **17**, 1825, DOI: **10.1021/acs.nanolett.6b05134**.

16 J. Reedijk and K. R. Poeppelmeier, *Comprehensive Inorganic Chemistry II: from Elements to Applications*, Elsevier, 2nd edn, 2013, p. 7544.

17 J. Polte, Fundamental growth principles of colloidal metal nanoparticles - a new perspective, *Crystengcomm*, 2015, **17**, 6809, DOI: **10.1039/c5ce01014d**.

18 N. Kapuria, M. Conroy, V. A. Lebedev, T. E. Adegoke, Y. Zhang, I. S. Amiinu, U. Bangert, A. Cabot, S. Singh and K. M. Ryan, Subsuming the Metal Seed to Transform Binary Metal Chalcogenide Nanocrystals into Multinary Compositions, *ACS Nano*, 2022, **16**, 8917.

19 N. Kapuria, S. Imtiaz, A. Sankaran, H. Geaney, T. Kennedy, S. Singh and K. M. Ryan, Multipod Bi(Cu2-xS)n Nanocrystals formed by Dynamic Cation–Ligand Complexation and Their Use as Anodes for Potassium-Ion Batteries, *Nano Lett.*, 2022, **22**, 10120, DOI: **10.1021/acs.nanolett.2c03933**.

20 N. Kapuria, N. N. Patil, K. M. Ryan and S. Singh, Two-dimensional copper based colloidal nanocrystals: synthesis and applications, *Nanoscale*, 2022, **14**, 2885, DOI: **10.1039/d1nr06990j**.

21 N. Kapuria, U. V. Ghorpade, M. Zubair, M. Mishra, S. Singh and K. M. Ryan, Metal chalcogenide semiconductor nanocrystals synthesized from ion-conducting seeds and their applications, *J. Mater. Chem. C*, 2020, **8**, 13868, DOI: **10.1039/d0tc02895a**.

22 B. A. Tappan, G. Barim, J. C. Kwok and R. L. Brutchey, Utilizing Diselenide Precursors toward Rationally Controlled Synthesis of Metastable CuInSe2 Nanocrystals, *Chem. Mater.*, 2018, **30**, 5704, DOI: **10.1021/acs.chemmater.8b02205**.

23 E. A. Hernandez-Pagan, E. H. Robinson, A. D. La Croix and J. E. Macdonald, Direct Synthesis of Novel Cu2-xSe Wurtzite Phase, *Chem. Mater.*, 2019, **31**, 4619, DOI: **10.1021/acs.chemmater.9b02019**.

24 J. M. Rhodes, C. A. Jones, L. B. Thal and J. E. Macdonald, Phase-Controlled Colloidal Syntheses of Iron Sulfide Nanocrystals via Sulfur Precursor Reactivity and Direct Pyrite Precipitation, *Chem. Mater.*, 2017, **29**, 8521, DOI: **10.1021/acs.chemmater.7b03550**.

25 B. A. Tappan, M. K. Horton and R. L. Brutchey, Ligand-Mediated Phase Control in Colloidal AgInSe2 Nanocrystals, *Chem. Mater.*, 2020, **32**, 2935, DOI: **10.1021/acs.chemmater.9b05163**.

26 J. J. Wang, A. Singh, P. Liu, S. Singh, C. Coughlan, Y. N. Guo and K. M. Ryan, Colloidal Synthesis of Cu2SnSe3 Tetrapod Nanocrystals, *J. Am. Chem. Soc.*, 2013, **135**, 7835, DOI: **10.1021/ja403083p**.

27 S. Singh and K. M. Ryan, Occurrence of Polytypism in Compound Colloidal Metal Chalcogenide Nanocrystals, Opportunities, and Challenges, *J. Phys. Chem. Lett.*, 2015, **6**, 3141, DOI: **10.1021/acs.jpclett.5b01311**.

28 J. Q. Geisenhoff, A. K. Tamura and A. M. Schimpf, Manipulation of Precursor Reactivity for the Facile Synthesis of Heterostructured and Hollow Metal Selenide Nanocrystals, *Chem. Mater.*, 2020, **32**, 2304, DOI: **10.1021/acs.chemmater.9b04305**.

29 M. S. Sokolikova, P. C. Sherrell, P. Palczynski, V. L. Bemmer and C. Mattevi, Direct solution-phase synthesis of 1T ' WSe2 nanosheets, *Nat. Commun.*, 2019, **10**, 712, DOI: **10.1038/s41467-019-08594-3**.

30 Z. Liu, K. Nie, X. Qu, X. Li, B. Li, Y. Yuan, S. Chong, P. Liu, Y. Li, Z. Yin and W. Huang, General Bottom-Up Colloidal Synthesis of Nano-Monolayer Transition-Metal Dichalcogenides with High 1T′-Phase Purity, *J. Am. Chem. Soc.*, 2022, **144**, 4863, DOI: **10.1021/jacs.1c12379**.

31 J. N. Yang, Q. C. Xu, Y. T. Zheng, Z. M. Tian, Y. Y. Shi, C. X. Ma, G. Y. Liu, B. Peng, Z. Wang and W. J. Zheng, Phase Engineering of Metastable Transition Metal Dichalcogenides via Ionic Liquid Assisted Synthesis, *ACS Nano*, 2022, **16**, 15215, DOI: **10.1021/acsnano.2c06549**.

32 L. Wu, Q. Wang, T. T. Zhuang, G. Z. Zhang, Y. Li, H. H. Li, F. J. Fan and S. H. Yu, A library of polytypic copper-based quaternary sulfide nanocrystals enables efficient solar-to-hydrogen conversion, *Nat. Commun.*, 2022, **13**, 5414, DOI: **10.1038/s41467-022-33065-7**.

33 S. Das, G. Swain and K. Parida, One step towards the 1T/2H-MoS2 mixed phase: a journey from synthesis to application, *Mater. Chem. Front.*, 2021, **5**, 2143, DOI: **10.1039/d0qm00802h**.

34 P. Prabhu, V. Jose and J. M. Lee, Design Strategies for Development of TMD-Based Heterostructures in Electrochemical Energy Systems, *Matter*, 2020, **2**, 526, DOI: **10.1016/j.matt.2020.01.001**.

35 R. F. Zhou, Y. Zheng, M. Jaroniec and S. Z. Qiao, Determination of the Electron Transfer Number for the Oxygen Reduction Reaction: From Theory to Experiment, *ACS Catal.*, 2016, **6**, 4720, DOI: **10.1021/acscatal.6b01581**.

36 S. Abinaya, P. Moni, V. Parthiban, A. K. Sahu and M. Wilhelm, Metal Silicide Nanosphere Decorated Carbon-Rich Polymer-Derived Ceramics: Bifunctional Electrocatalysts towards Oxygen and their Application in Anion Exchange Membrane Fuel Cells, *Chemelectrochem*, 2019, **6**, 3268, DOI: **10.1002/celc.201900475**.

37 B. Shang, X. Q. Cui, L. Jiao, K. Qi, Y. W. Wang, J. C. Fan, Y. Y. Yue, H. Y. Wang, Q. L. Bao, X. F. Fan, S. T. Wei, W. Song, Z. L. Cheng, S. J. Guo and W. T. Zheng, Lattice -Mismatch-Induced Ultrastable 1T-Phase MoS2-Pd/Au for

Plasmon-Enhanced Hydrogen Evolution, *Nano Lett.*, 2019, **19**, 2758, DOI: 10.1021/acs.nanolett.8b04104.

38 Y. Y. Liu, J. J. Wu, K. P. Hackenberg, J. Zhang, Y. M. Wang, Y. C. Yang, K. Keyshar, J. Gu, T. Ogitsu, R. Vajtai, J. Lou, P. M. Ajayan, B. C. Wood and B. I. Yakobson, Self-optimizing, highly surface-active layered metal dichalcogenide catalysts for hydrogen evolution, *Nat. Energy*, 2017, **2**, 17127, DOI: 10.1038/nenergy.2017.127.

39 J. W. Thomson, K. Nagashima, P. M. Macdonald and G. A. Ozin, From Sulfur-Amine Solutions to Metal Sulfide Nanocrystals: Peering into the Oleylamine-Sulfur Black Box, *J. Am. Chem. Soc.*, 2011, **133**, 5036, DOI: 10.1021/ja1109997.

40 R. L. Brutchey, Diorganyl Dichalcogenides as Useful Synthons for Colloidal Semiconductor Nanocrystals, *Acc. Chem. Res.*, 2015, **48**, 2918, DOI: 10.1021/acs.accounts.5b00362.

41 B. C. Steimle, R. W. Lord and R. E. Schaak, Phosphine-Induced Phase Transition in Copper Sulfide Nanoparticles Prior to Initiation of a Cation Exchange Reaction, *J. Am. Chem. Soc.*, 2020, **142**, 13345, DOI: 10.1021/jacs.0c06602.

42 G. Frenking, I. Fernandez, N. Holzmann, S. Pan, I. Krossing and M. F. Zhou, Metal-CO Bonding in Mononuclear Transition Metal Carbonyl Complexes, *JACS Au*, 2021, **1**, 623, DOI: 10.1021/jacsau.1c00106.

43 A. L. Washington, M. E. Foley, S. Cheong, L. Quffa, C. J. Breshike, J. Watt, R. D. Tilley and G. F. Strouse, Ostwald's Rule of Stages and Its Role in CdSe Quantum Dot Crystallization, *J. Am. Chem. Soc.*, 2012, **134**, 17046, DOI: 10.1021/ja302964e.

44 G. P. Gao, Y. Jiao, F. X. Ma, Y. L. Jiao, E. Waclawik and A. J. Du, Charge Mediated Semiconducting-to-Metallic Phase Transition in Molybdenum Disulfide Monolayer and Hydrogen Evolution Reaction in New 1T' Phase, *J. Phys. Chem. C*, 2015, **119**, 13124, DOI: 10.1021/acs.jpcc.5b04658.

45 S. Jayabal, G. Saranya, J. Wu, Y. Q. Liu, D. S. Geng and X. B. Meng, Understanding the high-electrocatalytic performance of two-dimensional MoS2 nanosheets and their composite materials, *J. Mater. Chem. A*, 2017, **5**, 24540, DOI: 10.1039/c7ta08327k.

46 Y. Cao, Roadmap and Direction toward High-Performance MoS2 Hydrogen Evolution Catalysts, *ACS Nano*, 2021, **15**, 11014, DOI: 10.1021/acsnano.1c01879.

47 J. Q. Zhu, Z. C. Wang, H. J. Dai, Q. Q. Wang, R. Yang, H. Yu, M. Z. Liao, J. Zhang, W. Chen, Z. Wei, N. Li, L. J. Du, D. X. Shi, W. L. Wang, L. X. Zhang, Y. Jiang and G. Y. Zhang, Boundary activated hydrogen evolution reaction on monolayer MoS2, *Nat. Commun.*, 2019, **10**, 1348, DOI: 10.1038/s41467-019-09269-9.

48 Y. Lee, N. Ling, D. Kim, M. Zhao, Y. A. Eshete, E. Kim, S. Cho and H. Yang, Heterophase Boundary for Active Hydrogen Evolution in MoTe2, *Adv. Funct. Mater.*, 2022, **32**, 2105675, DOI: 10.1002/adfm.202105675.

49 X. Y. Lu, Y. Yang, Y. Yin, Z. L. Wang, L. Sutrisno, C. L. Yan and O. G. Schmidt, Atomic Heterointerface Boosts the Catalytic Activity toward Oxygen Reduction/Evolution Reaction, *Adv. Energy Mater.*, 2021, **11**, 2102235, DOI: 10.1002/aenm.202102235.

50 J. N. Song, Y. Chen, H. J. Huang, J. J. Wang, S. C. Huang, Y. F. Liao, A. E. Fetohi, F. Hu, H. Y. Chen, L. L. Li, X. P. Han, K. M. El-Khatib and S. J. Peng, Heterointerface Engineering of Hierarchically Assembling Layered Double Hydroxides on Cobalt Selenide as Efficient Trifunctional Electrocatalysts for Water Splitting and Zinc-Air Battery, *Adv. Sci.*, 2022, **9**, 2104522, DOI: 10.1002/advs.202104522.

51 K. Huang, K. Bi, J. C. Xu, C. Liang, S. Lin, W. J. Wang, T. Z. Yang, Y. X. Du, R. Zhang, H. J. Yang, D. Y. Fan, Y. G. Wang and M. Lei, Novel graphite-carbon encased tungsten carbide nanocomposites by solid-state reaction and their ORR electrocatalytic performance in alkaline medium, *Electrochim. Acta*, 2015, **174**, 172, DOI: 10.1016/j.electacta.2015.05.152.

52 G. Solomon, M. G. Kohan, M. Vagin, F. Rigoni, R. Mazzaro, M. M. Natile, S. J. You, V. Morandi, I. Concina and A. Vomiero, Decorating vertically aligned MoS2 nanoflakes with silver nanoparticles for inducing a bifunctional electrocatalyst towards oxygen evolution and oxygen reduction reaction, *Nano Energy*, 2021, **81**, 105664, DOI: 10.1016/j.nanoen.2020.105664.

53 J. X. Mao, P. Liu, C. C. Du, D. X. Liang, J. Y. Yan and W. B. Song, Tailoring 2D MoS2 heterointerfaces for promising oxygen reduction reaction electrocatalysis, *J. Mater. Chem. A*, 2019, **7**, 8785, DOI: 10.1039/c9ta01321k.